International Journal of Thermal Sciences 212 (2025) 109783

Contents lists available at ScienceDirect

International Journal of Thermal Sciences

journal homepage: www.elsevier.com/locate/ijts

A numerical study of blockage and inclination effects on natural convection in a uniformly heated air flow channel

Siyu Ji, Quang Duy Nguyen, Yixiang Gan, Chengwang Lei *

Centre for Wind, Waves and Water, School of Civil Engineering, The University of Sydney, Sydney, NSW 2006, Australia

ARTICLE INFO

Keywords:
Natural convection
Thermal boundary layer
Uniform heating
Blockage effects
Inclined channel

ABSTRACT

The present study is concerned with the flow behaviour and thermal performance of an air flow channel subject to uniform heating with an adiabatic circular cylinder symmetrically positioned in the channel. A two-dimensional numerical study is conducted, covering a range of blockage ratios (β, the ratio between the cylinder diameter to the channel width), inclination angles (φ, relative to horizontal plane), cylinder positions (h, the distance from the inlet), and Rayleigh numbers (Ra, up to 6.0×10^{11}). It is observed that vortices shed from the cylinder interact with the thermal boundary layers (TBLs) adjacent to channel walls, which disturbs downstream TBLs and enhances mixing in the channel. For $Ra = 6.0 \times 10^{11}$, the averaged lateral wall temperature of a vertical channel ($\varphi = 90°$) drops by 31 % at $\beta = 0.50$, and the mass flow rate through the channel increases by 40 % at $\beta = 0.25$ compared to an unblocked vertical channel (i.e., without the cylinder). In a channel inclined at $\varphi = 30°$, up to 29 % reduction of the averaged wall temperature is achieved compared to an unblocked inclined channel at $Ra = 6.0 \times 10^{11}$. However, the inclination of the channel from the vertical position generally deteriorates its thermal performance. Moreover, at $\beta = 0.75$ and $Ra = 6.0 \times 10^{11}$, the flow skews towards one lateral wall at $\varphi = 30°$ and 90°, resulting in an irregular wake, but the flow structures are more symmetric at $\varphi = 60°$. The results reported here provide a passive strategy to design obstacles in convective flow channels for optimising thermal performance.

1. Introduction

Over recent decades, extensive research has focused on enhancing the efficiency of natural convection systems due to their relatively low heat-dissipating rates. In general, the state of the thermal boundary layer (TBL) forming adjacent to a heat transfer surface determines the thermal performance of a natural convection system. Therefore, understanding the properties and behaviours of the TBL may facilitate predicting and controlling the performance of a heat transfer surface. Advanced techniques, including passive, active, and compound strategies, have been developed to enhance heat transfer by natural convection. Compared to active strategies, passive strategies are advantageous in terms of reliability and sustainability [1].

A specific passive strategy of interest is by inserting a vortex generator in a heated channel, which may disturb thermal flow and induce TBL instability. The mechanism is analogous to enhancing flow mixing by disturbing the velocity boundary layer in non-thermal flows. Extensive studies have been conducted on non-thermal flows past bluff bodies. A typical configuration includes a circular cylinder placed between two parallel walls with a finite lateral separation, or within a channel. This configuration is referred as "a confined flow past a circular cylinder" or "a flow past a confined circular cylinder" [2]. In this configuration, the presence of the cylinder results in alternating shedding of vortices from the cylinder, which forms a reverse von Kármán vortex street and may induce wake flow transition from laminar to turbulence. It has been reported in the comprehensive review of Nguyen et al. [2] that the flow behaviour and vortex shedding forming behind a confined cylinder strongly depend on the blockage ratio, the ratio of the cylinder diameter to the spacing between the two lateral walls, that is, $\beta = D/W$, where β is the blockage ratio, D is the diameter of the cylinder, and W is the width of the channel. They reported that the hydrodynamic properties of the cylinder, including the Strouhal number (St), lift and drag coefficients grow rapidly with increasing blockage ratio.

The findings obtained in non-thermal flows have been utilised to enhance heat transfer in thermal flows due to induced flow instability and enhanced mixing caused by blockage effects. For instance, Sparrow and Pfeil [3] experimentally tested 15 different configurations of a heated horizontal cylinder confined in a vertical channel. The Rayleigh

* Corresponding author.
E-mail address: chengwang.lei@sydney.edu.au (C. Lei).

https://doi.org/10.1016/j.ijthermalsci.2025.109783
Received 22 November 2024; Received in revised form 30 January 2025; Accepted 5 February 2025
Available online 13 February 2025
1290-0729/© 2025 The Authors. Published by Elsevier Masson SAS. This is an open access article under the CC BY-NC-ND license (http://creativecommons.org/licenses/by-nc-nd/4.0/).

numbers are in the range of 1.5×10^4 to 2×10^5. They measured the temperature distribution along the channel walls and reported that the temperature profiles are highly dependent on the conductivity of the walls. They also emphasised that there was no heat transfer enhancement when the blockage ratio was smaller than 0.1. This result contradicted that reported by Marsters [4], who conducted an experimental study with Ra varying from 10 to 5×10^5. Their experimental setup included a heated cylinder confined by two vertical walls with adjustable wall heights (H/D from 5 to 128) and blockage ratios (D/W from 0 to 0.50, where $D/W \to 0$ is the no-wall case). Their results showed that with the presence of the lateral walls, the enhancement of heat transfer is considerable, even at very low blockage ratios (e.g., 30 % enhancement at a blockage ratio of 0.05). Karim et al. [5] found that the heat transfer from a heated cylinder can be enhanced by confining the flow using two non-conductive walls. They conducted experiments at various blockage ratios (from no confinement to $\beta = 2/3$) to examine natural convective heat transfer from a horizontal isothermally heated cylinder between two vertical walls for Rayleigh numbers from 2×10^3 to 3×10^5. They reported that increasing the blockage ratio results in an increase of heat transfer enhancement. More recently, Mathis et al. [6] examined the blockage effects on a convective flow channel, which comprises an adiabatic circular cylinder symmetrically confined by two isothermal walls. They reported significant heat transfer enhancement up to 41.9 % at $\beta = 0.45$. Nguyen et al. [7] conducted a systematic investigation of the blockage effect under a similar setup and reported up to 64.3 % heat transfer enhancement at $\beta = 0.50$.

Heat transfer through inclined channels has also been studied extensively. Azevedo and Sparrow [8] experimentally investigated the impacts of the channel width and inclination angle on laminar natural convection in an unblocked channel. They established correlations between the Nusselt number (Nu), Rayleigh number (Ra), inclination angle, and the channel's aspect ratio for three different heating modes. The presence of a secondary flow and recirculation zones when Ra exceeded a certain threshold was reported. Manca et al. [9] studied the influence of the inclination angle on the thermal performance of channels heated by constant heat flux. They reported that inclining the channel from the vertical position deteriorates the channel's thermal performance. More recently, Talukdar et al. [10] conducted numerical simulations to determine the transition characteristics in a natural convective air flow channel subject to uniform heating at $5.93 \times 10^6 \leq Ra \leq 1.45 \times 10^9$. The channel is inclined from 30° to 90° relative to the horizontal plane. Periodical single-roll longitudinal vortices are observed, and the formation of which is identified to characterise flow transition. Zhang and Samtaney [11] considered an isothermally heated circular cylinder in a forced convection air flow channel with adiabatic lateral walls to investigate the inclination effect on the flow behaviour and heat transfer. The geometrical configuration is similar to utilising the cylinder as a vortex generator to disturb the TBL and enhance flow mixing considered in the study of Nguyen et al. [7].

Despite the thermal flow in wall-cylinder systems and inclined channels have been examined for decades, to the best of our knowledge, a partly blocked and inclined convective flow channel subject to uniform heating has not been considered in the literature. From engineering application perspective, it is important to understand how flow blockage and channel inclination affect the flow behaviour and consequent thermal performance of a uniformly heated channel, and how to optimise the strategy for best performance. This motivates the present study, which is concerned with the effects of blockage ratio, channel inclination, and the cylinder position at different Rayleigh numbers.

2. Numerical details

2.1. Computational domain and numerical procedures

In this study, an air flow channel with uniformly and symmetrically heated lateral walls is considered. A circular cylinder is inserted along the centreline of the channel at a distance (h) measured from the channel inlet (refer to Fig. 1). The aspect ratio of the channel is fixed at $A = H/W = 14.3$. Other major geometric parameters are listed in Table 1. To avoid potential confusion, we refer to the left/upper wall as "Wall A" and the right/bottom wall as "Wall B", respectively.

The buoyancy-driven flow under the effect of a constant heat flux is characterised by the Rayleigh number (Ra) and Prandtl number (Pr), which are defined as follows:

$$Ra = \frac{g\alpha q_w'' H^4}{k\nu a}, Pr = \frac{\nu}{a}, \tag{1}$$

where α and ν are the thermal expansion coefficient and kinematic viscosity of the fluid, respectively. $a = k/(\rho c_p)$ is the thermal diffusivity of the fluid, k, ρ and c_p are the thermal conductivity, density, and specific heat capacity of the fluid, respectively. The range of Ra varies from 6.0×10^9 to 6.0×10^{11}, and the Prandtl number is fixed at 0.7 in this study.

A two-dimensional (2-D) numerical study is carried out to investigate the natural convection flow behaviour in the channel. Justification for adopting the 2-D model will be presented later in this section. The Navier-Stoke equations and energy equation describing the thermal flow in the channel are written in a dimensional form as below:

$$\frac{\partial \rho}{\partial t} + \nabla \bullet (\rho \boldsymbol{V}) = 0, \tag{2}$$

$$\frac{\partial(\rho u)}{\partial t} + \nabla \bullet (\rho u \boldsymbol{V}) = -\frac{\partial p}{\partial x} + \frac{\partial}{\partial x}\left(-\frac{2}{3}\mu \bullet \nabla \boldsymbol{V} + 2\mu \frac{\partial u}{\partial x}\right) + \frac{\partial}{\partial y}\left[\mu\left(\frac{\partial v}{\partial x} + \frac{\partial u}{\partial y}\right)\right] + \rho g \cos\varphi, \tag{3}$$

$$\frac{\partial(\rho v)}{\partial t} + \nabla \bullet (\rho v \boldsymbol{V}) = -\frac{\partial p}{\partial y} + \frac{\partial}{\partial x}\left[\mu\left(\frac{\partial v}{\partial x} + \frac{\partial u}{\partial y}\right)\right] + \frac{\partial}{\partial y}\left(-\frac{2}{3}\mu \bullet \nabla \boldsymbol{V} + 2\mu \frac{\partial v}{\partial y}\right) + \rho g \sin\varphi, \tag{4}$$

$$\frac{\partial(\rho c_p T)}{\partial t} + \nabla \bullet (\rho c_p T \boldsymbol{V}) = \nabla \bullet (k \nabla T), \tag{5}$$

where u and v are the velocity components in the transverse and longitudinal directions, respectively. p, t and T are the pressure, time and temperature, respectively. The governing equations are solved with the ideal gas law for air, that is, $p = \rho RT$, where R is the gas constant. The

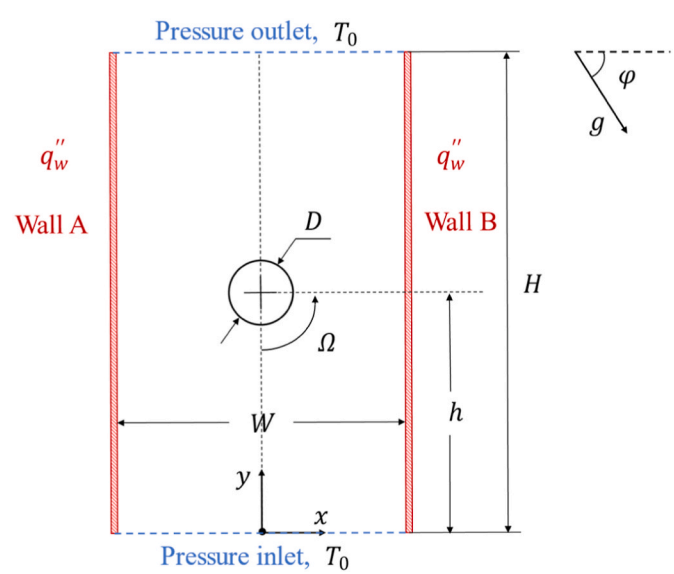

Fig. 1. Sketch of the computational domain. g indicates the direction of gravity; and Ω denotes the angular position along the circumference of the cylinder.

Table 1
Definitions and values of key geometric parameters.

Symbol	Parameter	Values
β	Blockage ratio, $\beta = D/W$	0.25, 0.50, 0.75
h^*	Longitudinal position of the cylinder, $h^* = h/H$	0.05, 0.25, 0.50
φ	Inclination angle	30°, 60°, 90°

dimensional quantities u, v, x, y, p, t, T are normalised to obtain the dimensionless quantities u^*, v^*, x^*, y^*, p^*, t^* and θ as follows [12]:

$$\left.\begin{aligned} x^* &= \frac{x}{W}, y^* = \frac{y}{H}, \\ u^* &= \frac{u}{\frac{a}{H}(RaPr)^{2/5}}, v^* = \frac{v}{\frac{a}{H}(RaPr)^{2/5}}, \\ p^* &= \frac{p}{\rho\left(\frac{a}{H}\right)^2(RaPr)^{4/5}}, t^* = \frac{t}{\frac{H^2}{a}(RaPr)^{-2/5}}, \\ \theta &= \frac{T - T_0}{\frac{q_w^{''}H}{k}(RaPr)^{-1/5}} \end{aligned}\right\} \tag{6}$$

Note that different length scales are adopted to normalise the transverse and longitudinal coordinates. Hereinafter, u^*, v^*, x^*, y^*, p^*, t^*, and h^* are replaced by u, v, x, y, p, t and h for brevity.

No-slip boundary conditions are applied to the cylinder surface and the two lateral walls, and a constant heat flux $q_w^{''}$ is imposed on both channel walls. Pressure inlet and pressure outlet are prescribed at the channel inlet and outlet, respectively. The boundary conditions are expressed in the dimensionless form as follows:

- On the heated channel walls:

$$u = v = 0, \tag{7}$$

$$\frac{\partial\theta}{\partial x} = -\frac{1}{A}(RaPr)^{1/5} \tag{8}$$

- On the cylinder surface:

$$u = v = 0, \tag{9}$$

$$\frac{\partial\theta}{\partial x} = 0 \tag{10}$$

- At the channel inlet:

The inflow direction is assumed to be normal to the boundary, and the fluid is at the reference temperature. Furthermore, the gauge pressure is set to zero. That is,

$$\theta = 0, \tag{11}$$

$$p = -\frac{1}{2}|v|^2, \tag{12}$$

- At the channel outlet:

The flow is also assumed to be normal to the boundary. If $v \geq 0$, the fluid exits the channel. Otherwise, backflow occurs, and external fluid enters the channel at the reference temperature ($\theta = 0$). The boundary face pressure is calculated based on the velocity in the adjacent cell zone.

The SIMPLE Scheme for pressure-velocity coupling and the PRESTO! Scheme for pressure are employed to solve the governing equations [13]. The second-order upwind scheme is applied to advection terms.

As mentioned earlier, justification for adopting a 2-D numerical model is discussed here. It has been reported in the study of Chen et al. [14] that the transition of TBL from laminar to turbulence along a uniformly heated vertical plate occurs when Ra exceeds 2×10^{13}. For a uniformly heated vertical channel, Thebault et al. [15] observed a transition at $Ra = 1.5 \times 10^{12}$. They defined a temperature indicator h_T, which is the longitudinal position along the channel where the time-averaged wall temperature peaks before a sudden decrease downstream. Such wall temperature behaviour is due to heat transfer enhancement associated with TBL transition from laminar to turbulent state. It is anticipated that, within the range of Ra considered in the present study (6.0×10^9–6.0×10^{11}), the unblocked channel flow does not undergo the transition to turbulence. To verify this, a set of simulations is conducted for both vertical and inclined channels at Ra up to 6.0×10^{12}.

Fig. 2 (a) shows the time-averaged temperature profiles along the channel walls at different Ra in the vertical channel without blockage. For $Ra \leq 10^{11}$, the time-averaged temperature distributions grow monotonically along the wall. However, the temperature peaks at $h_T \approx 0.75$ at $Ra = 6.0 \times 10^{12}$, indicating that the TBL experiences a transition [15]. Fig. 2 (b) presents the time-averaged temperature distribution along both channel walls at $Ra = 6.0 \times 10^{11}$ for three different inclination angles ($\varphi = 30°, 60°, 90°$). A small deviation between the temperature profiles of the two channel walls is noticeable, which becomes more distinct with reducing inclination angle. However, no sign of TBL transition is observed from the wall-temperature profiles of the unblocked channel at Ra below 10^{12}. Although the presence of a cylinder in the channel may trigger flow instability and subsequent transition to three-dimensional flow, it is expected that the present 2-D model may capture the major features of the convective flow.

2.2. Dependency study

Dependency tests have been conducted to examine the sensitivity of the numerical solutions to the mesh resolution and time-step. The tests are conducted at the highest Rayleigh number of $Ra = 6.0 \times 10^{11}$. The mesh resolution is tested first for different blockage ratios and cylinder positions. Subsequently, the sensitivity to time-step is tested. For both mesh and time-step dependence tests, the calculations are extended for over 450 vortex-shedding cycles to ensure reliable statistics after the flow has reached a quasi-steady state. The temporarily and spatially averaged lateral wall temperature $\overline{\theta}_{wavg}$ and longitudinal velocity $\overline{v}_{in}$ at the inlet are calculated. In addition, the frequency f of temperature fluctuations at a monitoring point $(x, y) = (-0.43, 0.1)$ in the TBL behind the cylinder is examined.

Mesh refinement is focused on regions near the lateral walls, around the cylinder, and in the wake (within 10 D behind the cylinder). Other areas are progressively refined during this process. In particular, the first cell height off the heated channel wall L_m is subsequently reduced from the coarsest mesh to the finest mesh. A normalised cell height is defined as $L_m^* = L_m/\delta_T$, where $\delta_T \sim \frac{H}{(RaPr)^{1/5}}$ is the TBL thickness scale under isoflux conditions [12]. Hereinafter, L_m^* is replaced by L_m for brevity. The results of mesh resolution tests for $\beta = 0.50$ and $h = 0.05$ are presented in Table 2 as an example. Table 3 presents the results of the time-step tests for the same case, in which t_s is the normalised time-step size.

In Tables 2 and 3, the percentages in brackets represent the differences between the test cases relative to the reference cases (M4 and TS4 for mesh and time-step dependence tests respectively). It is seen in these tables that the variations of the monitored parameters obtained with different mesh resolutions and time-steps are within 1.5 % except for the coarsest mesh M1. Based on these dependency tests, the mesh M3 with the time-step TS3 have been selected for subsequent calculations.

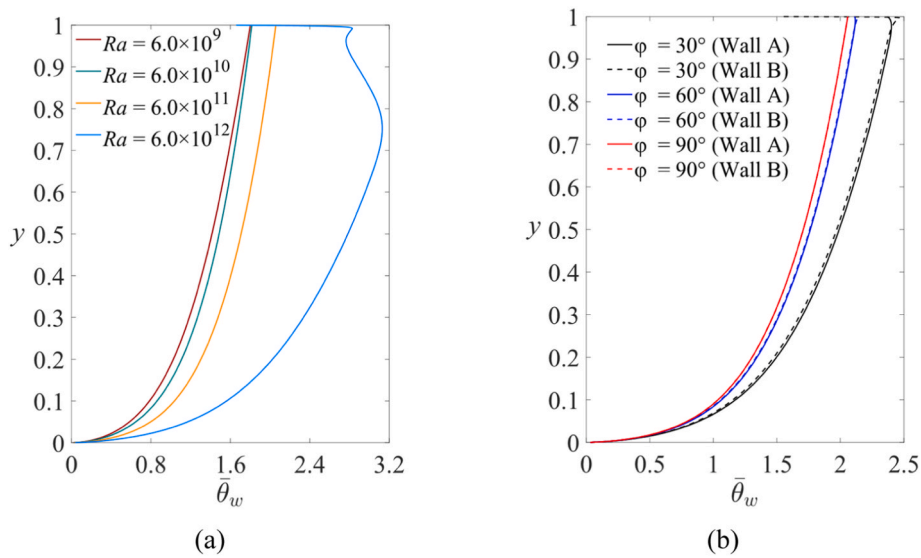

Fig. 2. Time-averaged temperature profiles in an unblocked channel along (a) wall A at different Rayleigh numbers; and (b) along both walls at different inclination angles for $Ra = 6.0 \times 10^{11}$.

Table 2
Mesh dependence test results for $\beta = 0.50$, $h = 0.05$, and $Ra = 6.0 \times 10^{11}$ ($t_s = 0.010$).

Mesh	L_m	No. of elements	$\bar{\theta}_{wavg}$	$\bar{v}_{in}$	f
M1	0.143	15,672	1.171 (3.44 %)	0.2907 (−2.17 %)	3.587 (−2.96 %)
M2	0.071	28,300	1.144 (1.01 %)	0.2957 (−0.50 %)	3.666 (−0.83 %)
M3	0.036	51,298	1.118 (−1.38 %)	0.2970 (−0.06 %)	3.697 (−0.02 %)
M4	0.018	103,216	1.133	0.2971	3.696

Table 3
Time-step dependence test results for $\beta = 0.50$, $h = 0.05$, and $Ra = 6.0 \times 10^{11}$ ($L_m = 0.036$).

Time-step	t_s	$\bar{\theta}_{wavg}$	$\bar{v}_{in}$	f
TS1	0.010	1.118 (1.25 %)	0.2970 (0.25 %)	3.697 (0.52 %)
TS2	0.005	1.107 (0.28 %)	0.2967 (0.16 %)	3.717 (1.05 %)
TS3	0.003	1.105 (0.02 %)	0.2963 (0.04 %)	3.678 (0.00 %)
TS4	0.001	1.104	0.2962	3.678

2.3. Model validation

The validation of the numerical model includes two parts. First, the model is validated for pure natural convection in flow channels without blockage (Section 2.3.1), including a benchmark configuration described in Desrayaud et al. [16] and the experimental model reported in Thebault et, al. [15]. And second, the model is validated for mixed convection in a flow channel with blockage by a heated cylinder reported in Zhang and Samtaney [11] (Section 2.3.2). Further details are presented below.

2.3.1. Validation for natural convection in air flow channels without blockage

Two specific cases are simulated to validate the numerical model for natural convection in flow channels without blockage. First, the setup of a benchmark case described by Desrayaud et al. [16] is simulated. The above-mentioned pressure inlet and pressure outlet conditions are prescribed at the channel inlet and outlet respectively. The calculated Rayleigh number is 5×10^5, which is defined in terms of the channel width instead of channel length, and the aspect ratio of the channel is $A = 10$. Only one wall is partly heated between $h = 0.25$ and $h = 0.75$. The rest of the wall and the other wall are adiabatic. It is worth noting that, to make meaningful comparison with the literature, the velocity is normalised by a_0/W here [16], where a_0 is the thermal diffusivity of air at the reference temperature.

Fig. 3 depicts the time-averaged profiles of the streamwise velocity component at different horizontal sections of the channel. An excellent agreement between the present results and the benchmark data can be seen in this figure, which indicates that the present numerical model

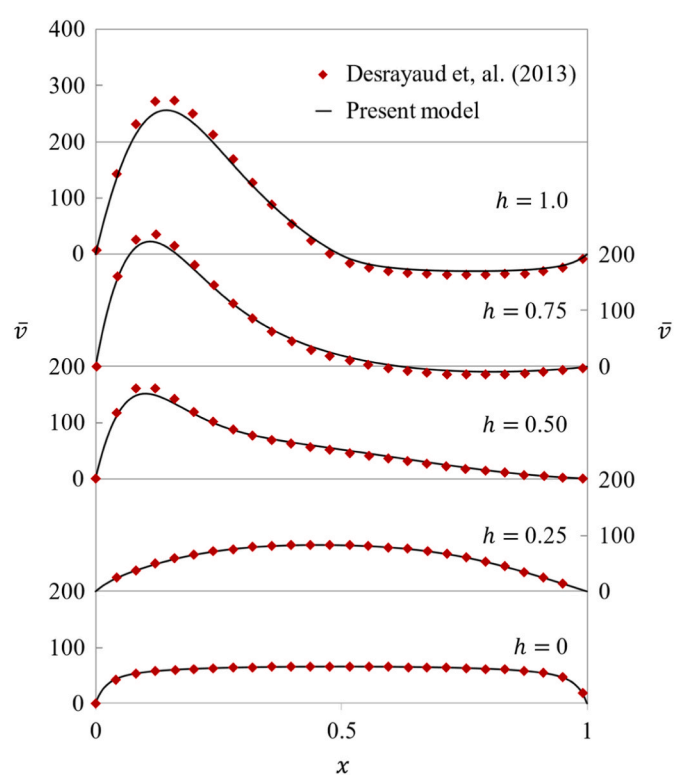

Fig. 3. Comparison of the streamwise velocity profile at different horizontal sections of the channel between the present model and the benchmark case in Desrayaud et al. [16].

including the adopted pressure inlet and pressure outlet boundary conditions is appropriate for simulating the natural convection flow in open channel systems.

Further, the experimental setup described in Thebault et, al. [15] is simulated. An air flow channel with an aspect ratio of $A = 15$ was considered in their experiment, and the Rayleigh number in terms of the channel length is $Ra = 3.5 \times 10^{12}$. Only one lateral wall of the channel is uniformly heated in the experiment, while the other wall is "passively heated" due to radiative transfer between the two lateral walls [15]. Accordingly, the Surface to Surface (S2S) radiation model is adopted in the simulation to account for radiation transfer. The thermal stratification of the ambient and the disturbances to the flow in the laboratory environment reported in the experiment are not considered in the numerical model.

Fig. 4 illustrates the comparison of the temperature profile at the channel outlet and the profile of the streamwise velocity component at $h = 0.25$ between the experimental data reported in Thebault et, al. [15] and those obtained with the present 2-D numerical model. Here, the temperature is scaled by the temperature difference based on the reported experimental data, i.e. $\overline{\theta}_{out} = (T - T_0)/(T_{max} - T_0)$. The velocity is normalised by the same scale as Equation (6). A reasonable agreement between the numerical and experimental data can be seen in Fig. 4. However, discrepancies between the two studies are also clear, which are attributed to multiple factors. First, the present numerical model is two-dimensional, whereas the experiment was three-dimensional. Second, the Rayleigh number considered in the experiment was in the flow regime in which transition from laminar to turbulence is expected to occur [15], but a laminar model is adopted here. And finally, the experiment involved a stratified ambient and environmental perturbations, which are not considered in the numerical model. It is worth noting that Thebault et, al. [15] also reported difficulties in matching their LES (large eddy simulation) model results with the experiment.

The above validations suggest that the present 2-D numerical model can be used to calculate laminar natural convection flows in open channels with confidence.

2.3.2. Validation for mixed convection in a partly blocked channel

To validate the present numerical model for convective flows through a partly blocked channel, mixed convection in an air flow channel reported in Zhang and Samtaney [11] is simulated. The configuration involved flow past an isothermally heated circular cylinder confined by two adiabatic lateral walls in an inclined channel. The present computational domain is extended to $H = 60D$ with $h = 10D$ to match that considered by Zhang and Samtaney [11]. The cylinder surface is defined as a no-slip boundary and is heated at a constant temperature T_c. A fully developed flow condition is applied at the inlet in which the velocity profile of $v(y) = 1.5v_{in}\left[1 - \left(\frac{2x}{W}\right)^2\right]$ is imposed. Outflow condition is prescribed at the outlet and no-slip conditions are applied to the lateral channel walls. The selected cases for validation include inclination angles of 0° (horizontal) and 90° (vertical). The simulations are performed at a Reynolds number (Re) of 100 and a Richardson number (Ri) of 1. The Reynolds and Richardson numbers are defined as:

$$Re = \frac{v_{in}D}{\nu}, \tag{13}$$

$$Ri = \frac{Ra}{Pr \times Re^2}, \tag{14}$$

The parameters evaluated for validation include the Strouhal number ($St = \frac{fD}{v_{in}}$), the spatially-temporally averaged Nusselt number along the cylinder surface ($\overline{Nu}_{avg} = \frac{h_c D}{k}$, where h_c is the convective heat transfer coefficient), and the fluctuating (root-mean-square, RMS) Nusselt number (Nu_{rms}). Table 4 depicts a comparison of the results obtained from the present model with those from Zhang and Samtaney [11]. It is observed that the flow in the vertical channel is steady at $Ri = 1$, and the parameters indicating flow fluctuations are zero or very close to zero. Accordingly, only the results for the horizontal channel are presented in this table. It should be noted that, for this validation, the thermal properties of air are obtained at the film temperature of $T_f = (T_c + T_0)/2$. The percentages given in brackets indicate the variations between the results obtained from this study and those from Zhang and

Table 4
Comparison of the mean and RMS of Nu and St in the horizontal channel.

	Zhang and Samtaney (2024)	Present study
$\overline{Nu}_{avg}$	6.410	5.925 (−7.56 %)
Nu_{rms}	0.026	0.025 (−1.61 %)
St	0.300	0.302 (−0.53 %)

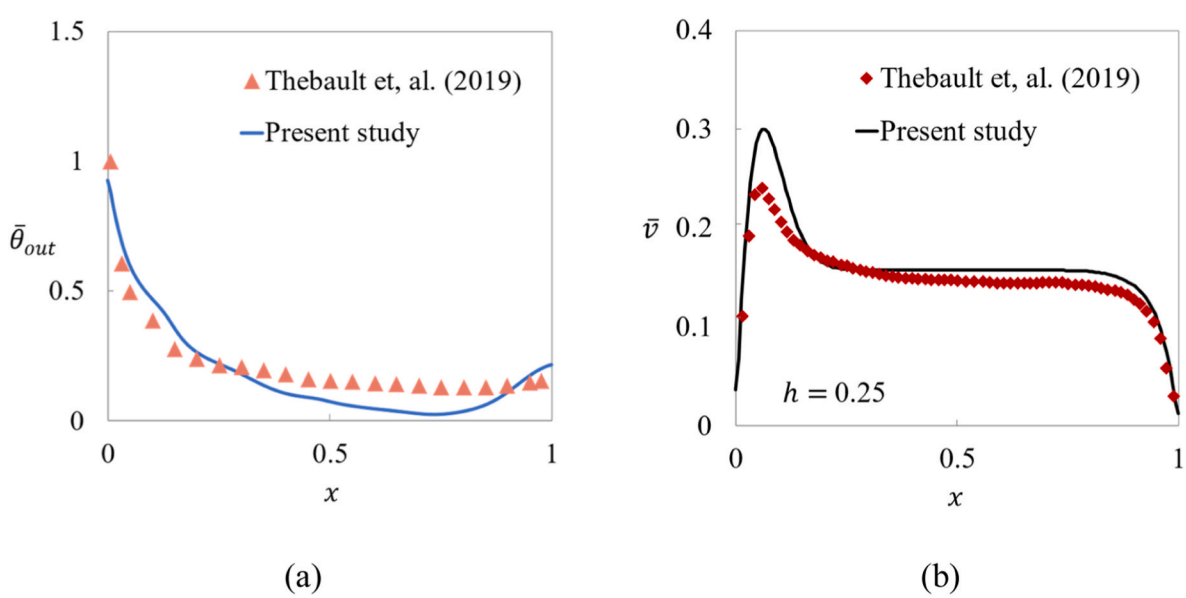

Fig. 4. Comparison of the (a) temperature profile at the channel outlet and (b) the profile of the streamwise velocity component at $h = 0.25$ between the experimental data in Thebault *et, al.* [15] and the present numerical model.

Samtaney [11]. It is seen in Table 4 that a reasonable agreement between the two studies is achieved.

Fig. 5 presents the comparison of the time-averaged local Nusselt number ($Nu_{loc,avg}$) distributions along the cylinder surface between the present results and those from Zhang and Samtaney [11] for both horizontal and vertical channels. Here Ω denotes the angular position along the surface of the cylinder, which is defined in Fig. 1. It is seen that a very good agreement is achieved. Therefore, the present numerical model is validated.

3. Results and discussions

Both qualitative (Section 3.1) and quantitative (Section 3.2) data are presented below to illustrate the effects of flow blockage and associated parameters on the convective flow in the channel. Section 3.1 focuses on qualitative observation of the thermal flow behaviour and corresponding flow mechanism, and Section 3.2 shows the impact of flow blockage on the channel wall temperature and mass flow rate through the channel.

3.1. Observation of thermal flow behaviour and flow mechanism

This subsection is organised as follows: Sections 3.1.1 ~ 3.1.3 focus on the cases with the cylinder placed at a fixed longitudinal position of $h = 0.05$. The effects of the cylinder position are discussed in Section 3.1.4. Further, Sections 3.1.1 and 3.1.2 are based on vertical channels, whereas the effects of inclination are discussed in Section 3.1.3.

3.1.1. Wake dynamics and mean flow behaviour

Fig. 6 (a) shows instantaneous vorticity contours in a vertical channel at different blockage ratios for $Ra = 6.0 \times 10^{11}$. It is observed that at the blockage ratios of 0.25 and 0.50, the flow undergoes a Hopf bifurcation, transitioning to an unsteady periodic state, in which the wall vortices periodically merge with those from the separated shear layers. As a result, a reversed von Kármán vortex street is present behind the cylinder, which is similar to the behaviour observed in a non-thermal flow (also known as "crisscross motion of vortex") [17].

Fig. 6 (b) shows instantaneous vorticity contours at the largest blockage ratio $\beta = 0.75$ for different Rayleigh numbers. It is seen that at this blockage ratio the presence of the lateral walls dramatically influences the formation of the vortices in the wake. At the lowest Rayleigh number of $Ra = 6.0 \times 10^{9}$, vortex shedding maintains a regular periodic pattern. However, at $Ra = 6.0 \times 10^{10}$ and 6.0×10^{11}, the flow appears to be approximately symmetric in the near wake, but the symmetry quickly breaks down, and the periodic vortex shedding is suppressed downstream. It is also observed that the wake flow randomly skews toward one of the lateral walls at $Ra = 6.0 \times 10^{11}$. Flow asymmetry and suppression of reversed von Kármán vortex street are also reported by Nguyen et al. [7] in an isothermally heated vertical channel at $\beta = 0.75$ for $Ra_T > 8.9 \times 10^{7}$ (where Ra_T is the isothermal Rayleigh number, $Ra_T = \frac{g\alpha\Delta T H^3}{\nu a}$). They found that the wake arbitrarily skews toward either side of the lateral walls at this blockage ratio. In non-thermal flows, Sahin and Owens [18] reported that the flow is globally asymmetric at $\beta = 0.7$, i.e., the time-averaged flow is asymmetric. The asymmetric structures in the wake of non-thermal confined flows have been systematically reviewed by Nguyen et al. [2]. One possible explanation of the occurrence of asymmetric flow structures is that the separated shear layer is elongated at such large blockage ratios, which may contribute to the suppression of periodic vortex shedding [19,20].

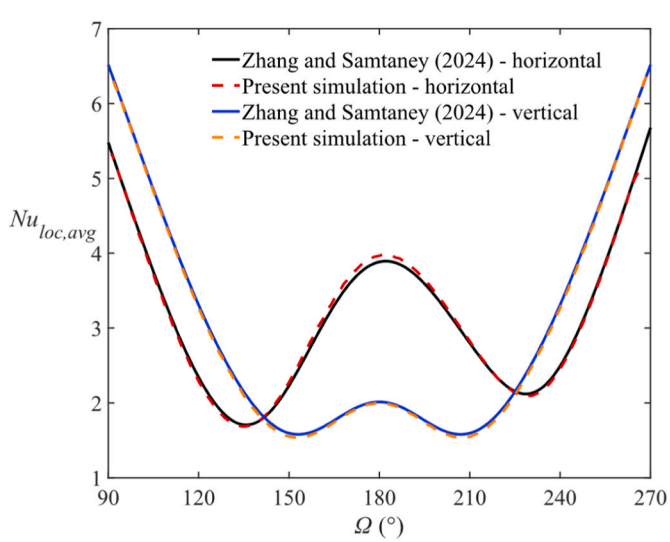

Fig. 5. Comparison of time-averaged Nu distribution along the cylinder surface between the validation and reference cases at $\beta = 0.25$, $Re = 100$, and $Ri = 1$.

Fig. 7 illustrates the contours of time-averaged longitudinal velocity and streamlines at different blockage ratios ($\beta = 0$ represents an unblocked channel) for $Ra = 6.0 \times 10^{10}$ as a representative case. In the unblocked channel, the maximum longitudinal velocity occurs near the channel walls (that is, within TBLs). With the presence of the cylinder, the high-velocity region concentrates near the centre of the channel at all blockage ratios. This phenomenon is more pronounced at $\beta = 0.25$ and 0.50, where the high-velocity region extends further downstream along the centreline. The mechanism behind this behaviour can be explained as follows: In an unblocked channel, velocity boundary layers develop along with the TBLs, the highest velocity occurs near the wall due to the relatively strong buoyancy effects within the TBLs. The presence of the cylinder accelerates the flow through the gaps between the cylinder and lateral walls. In the meantime, a low-pressure region forms behind the cylinder, leading to the formation of a recirculation zone, which is referred to as the vortex formation region [21]. The relatively low pressure in the vortex formation region causes the accelerated flows to merge near the centreline (refer to Fig. 6), resulting in a surge of the longitudinal velocity. As both the velocity boundary layers and wake continue to evolve further downstream, the velocities along the centreline and near-wall regions become increasingly comparable.

It is also very clear in Fig. 7 that larger blockage ratios lead to larger vortex formation regions. At the largest blockage ratio of $\beta = 0.75$, the cylinder obstructs the flow since the gaps between the cylinder and the channel walls are significantly reduced. As a result, jet flows are forming through the narrow gaps, which interact with the boundary layers adjacent to the lateral walls. These interactions in turn lead to shear layer separation and reattachment, forming large recirculation bubbles adjacent to the channel walls behind the cylinder location.

Fig. 8 depicts the time-averaged isotherms at different blockage ratios and streamlines at $\beta = 0.75$ for $Ra = 6.0 \times 10^{11}$. The blockage effect on the flow is clearly demonstrated in this figure. In general, the presence of the cylinder enhances flow mixing, resulting in relatively higher fluid temperatures downstream at all three blockage ratios. At the highest blockage ratio, the overall flow is slower through the channel due to the obstruction, leading to a considerably higher fluid temperature further downstream compared to that at lower blockage ratios ($\beta = 0.25, 0.50$). A high temperature zone is present near the wall behind the cylinder at $\beta = 0.75$ because heat is trapped by the recirculation bubbles described above. The asymmetric flow structure at $\beta = 0.75$ is also observed here. Clearly, the recirculation bubble near Wall A is much larger than that near Wall B, consistent with the wake asymmetry depicted in Fig. 6 (b).

3.1.2. Interactions between TBLs and cylinder wake

To understand the interactions between the thermal boundary layers and the cylinder wake, the temperature and transverse velocity fluctuations at multiple locations are monitored. At $Ra = 6.0 \times 10^{9}$, the flow is

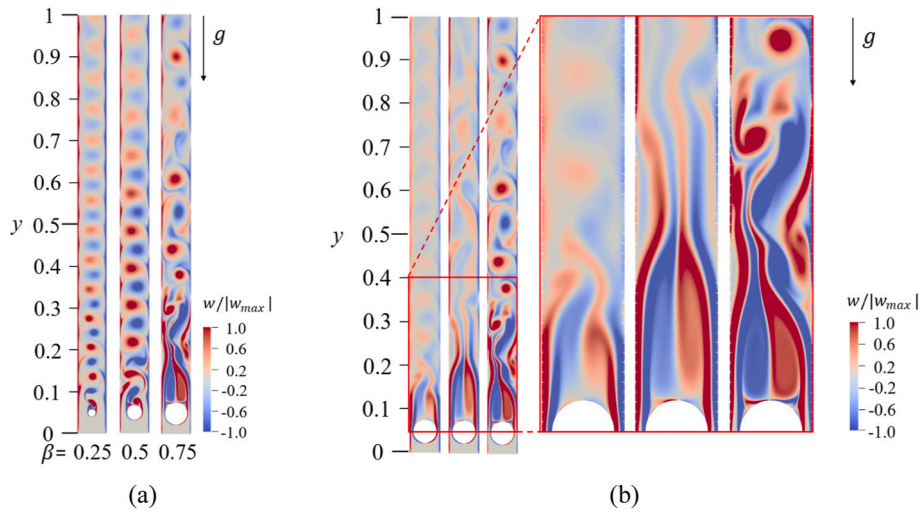

Fig. 6. Instantaneous vorticity contours of (a) $Ra = 6.0 \times 10^{11}$ at different blockage ratios; and (b) $\beta = 0.75$ for different Rayleigh numbers (left to fight: $Ra = 6.0 \times 10^{9}$, 6.0×10^{10}, 6.0×10^{11}).

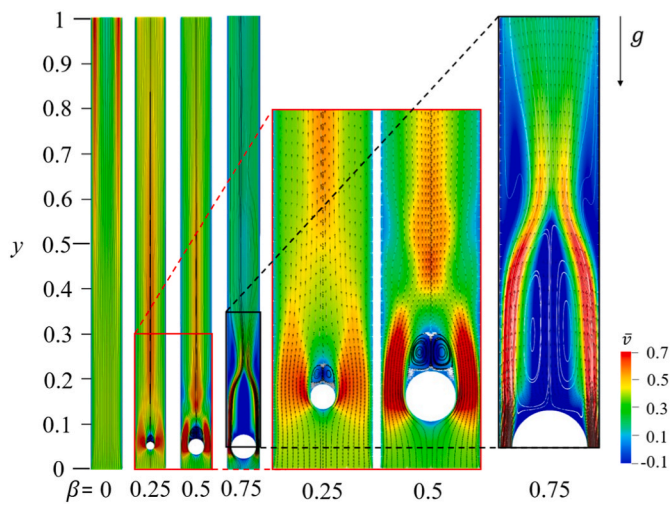

Fig. 7. Contours of time-averaged longitudinal velocity and streamlines at different blockage ratios ($\beta = 0.25, 0.50, 0.75$) for $Ra = 6.0 \times 10^{10}$ at $h = 0.05$.

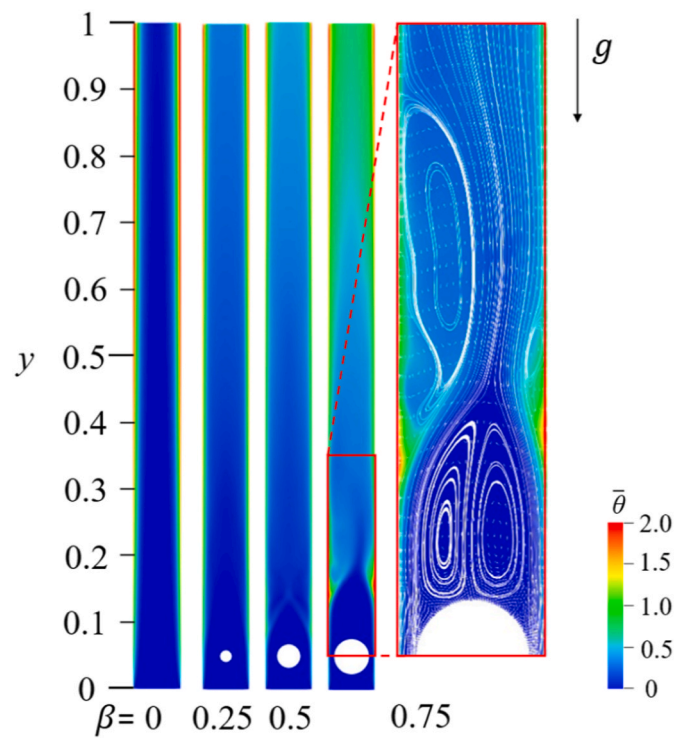

Fig. 8. Contours of time-averaged temperature ($\bar{\theta}$) at different blockage ratios and streamlines at $\beta = 0.75$ for $Ra = 6.0 \times 10^{11}$.

relatively stable at all blockage ratios. In contrast, the flow is very noisy with many disturbances at $Ra = 6.0 \times 10^{11}$. Therefore, the medium Rayliegh number of $Ra = 6.0 \times 10^{10}$ is considered in this section. Fig. 9 indicates the locations and coordinates of all monitoring points. Point ①~⑤ are in the TBL for monitoring temperature fluctuations; Point ⑥~⑨ are along the centreline in the cylinder wake for monitoring transverse velocity fluctuations; and Point ⑩ and ⑪ are in a shear layer separated from the cylinder surface, also for monitoring transverse velocity fluctuations. It is worth noting that the normalised TBL thickness in this case is estimated as $\frac{\delta_T}{W}$~0.11. Therefore, monitoring points ①~⑤ are located within the TBL (refer to Section 2.2 for the scale of δ_T).

Fig. 10 compares the spectral density of temperature fluctuations at Point ①~⑤ for different blockage ratios. It can be seen in Fig. 10 that at $\beta = 0.25$ and 0.50, a dominant frequency is detected throughout the TBL, indicating that the TBL is subject to periodic perturbations due to the presence of the cylinder (more details are given in Table 5 below). At $\beta = 0.50$, more higher-order harmonic frequencies appear in the downstream TBL beyond Point ③ compared to the situation at $\beta = 0.25$, suggesting that more small-scale thermal structures occur in the TBL. At the largest blockage ratio $\beta = 0.75$, jet flows form, resulting in more intense interactions between the TBL, separated shear layers, and the vortices in cylinder wake. At this blockage ratio, the dominant peak frequency disappears downstream (beyond Point ④), and a noisy spectrum is observed, indicating that the downstream TBL is experiencing a transition.

Fig. 11 illustrates the spectral density of transverse velocity fluctuations at Point ⑥~⑪ at $\beta = 0.50$. A dominant frequency and the corresponding harmonic frequencies can also be observed both in the cylinder wake and in the separated shear layer. In Fig. 11 (a), the higher frequency peaks gradually dimmish from the near wake to further downstream, indicating the small-scale structure in the cylinder wake disappears downstream (Point ⑨). However, in the separated shear layer, more frequency modes are observed at the position further away from the cylinder (Point ⑪) compared to the position close to the

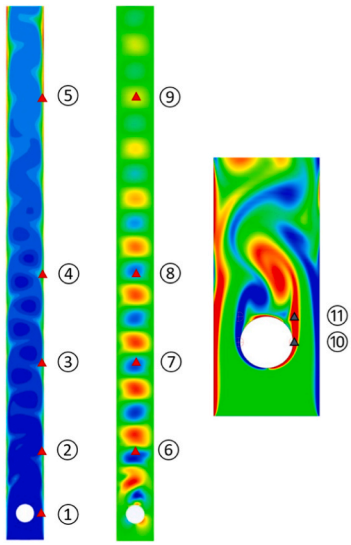

Monitoring points	Location	x	y
①	In the TBL	0.48	0.05
②			0.17
③			0.33
④			0.50
⑤			0.83
⑥	Along the centreline	0	0.17
⑦			0.33
⑧			0.50
⑨			0.83
⑩	In the separated shear layer	0.26	0.05
⑪			0.07

Fig. 9. Locations and coordinates of all monitoring points (indicated by filled triangles), where temperature and transverse velocity fluctuations are monitored.

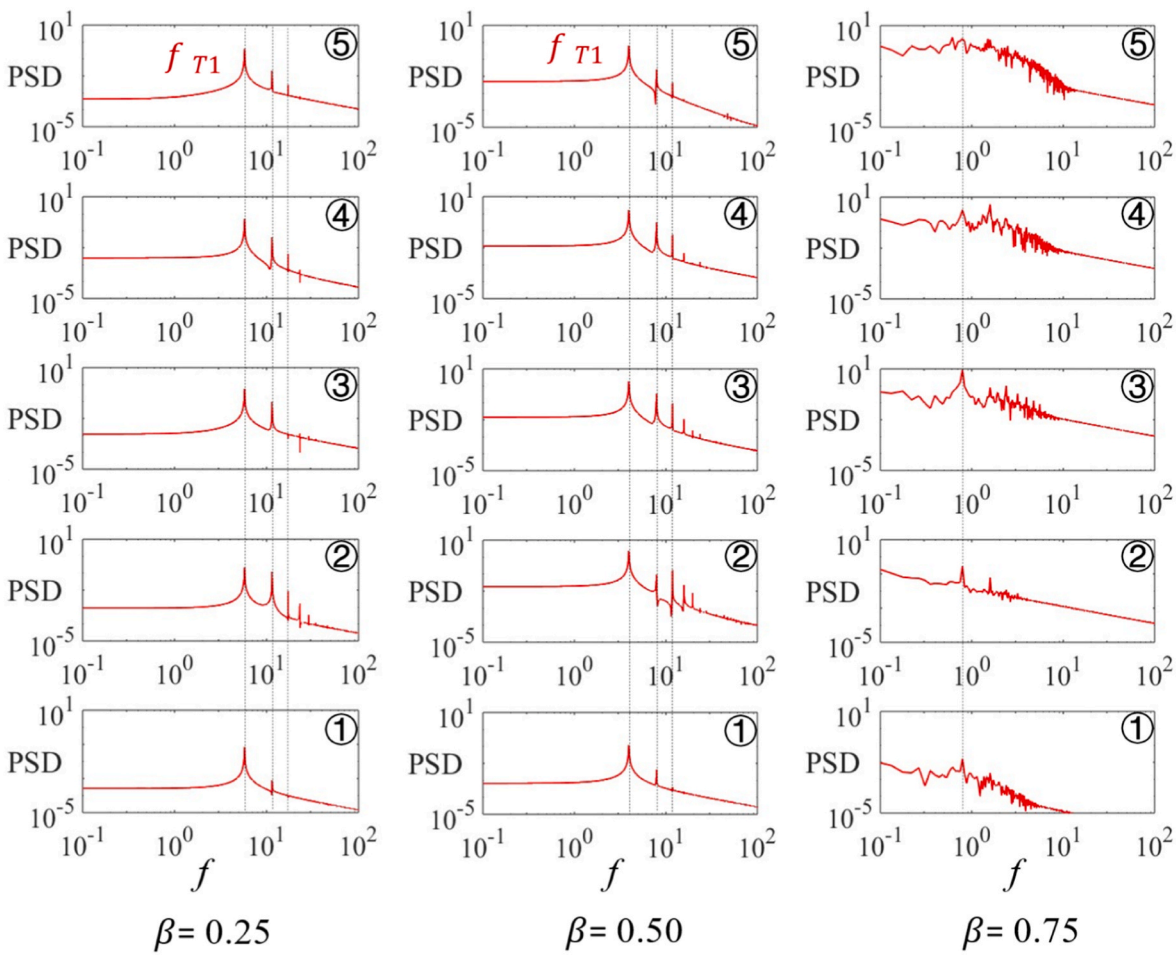

Fig. 10. Power spectra of temperature fluctuations at Points ① to ⑤ at different blockage ratios for $Ra = 6.0 \times 10^{10}$.

separation point of the shear layer (Point ⑩), indicating that more small-scale structures are associated with the development of the separated shear layers.

Table 5 displays the dominant frequencies and their harmonic components obtained at Points ③, ⑦, ⑪, respectively. The data in this table clearly confirms the strong interactions between the TBL, vortices in the wake, and the separated shear layer since certain frequencies repeatedly appear in all these flow structures. The most notable observation is that the same dominant frequency is observed in the TBL, the separated shear layer, and the wake, which suggests that the dominant frequency in the TBL is the same as the vortex shedding frequency. This is a result of the TBL being perturbed by vortex shedding forming from

Table 5
Dominant frequencies and their harmonic components in the TBL, the cylinder wake, and the separated shear layer.

Detected frequencies	TBL frequency f_T (at point ③)	Wake frequency f_W (at point ⑦)	Separated shear layer frequency f_{SL} (at point ⑪)
Dominant frequency, f_0	3.9	3.9	3.9
$2f_0$	7.9	/	7.9
$3f_0$	11.8	11.8	11.8
$4f_0$	15.7	/	15.7
$5f_0$	19.6	19.6	/

separated shear layers. The appearance of the higher-order harmonic frequencies indicates the presence of small-scale flow structures.

3.1.3. Effects of inclination

It is observed that, when the blockage ratio is relatively low (i.e., at $\beta = 0.25$ and 0.50), the flow behaviour appears very similar at different inclination angles, and no wake asymmetry is observed. However, at $\beta = 0.75$, the inclination has a considerable impact on the mean flow behaviour, causing the flow to change from an asymmetric structure in the vertical channel to a more symmetric structure at $\varphi = 60°$. Fig. 12 depicts the time-averaged isotherms and streamlines at $\beta = 0.75$ and different inclination angles for $Ra = 6.0 \times 10^{11}$. It is clear that the asymmetric structure of the flow observed in the vertical channel ($\varphi = 90°$) is influenced by the channel inclination. The mean flow structures at $\varphi = 30°$ and 90° are very similar. In both cases, the wake skews toward Wall B with a large recirculation bubble forming near Wall A and a smaller one near Wall B. However, the mean flow becomes more symmetric at $\varphi = 60°$.

To further investigate the impact of inclination on the asymmetric flow, the time-series of longitudinal velocities at a monitoring point $(x, y) = (0, 0.1)$ in the near wake and the corresponding instantaneous vorticity contours are plotted in Fig. 13. Here, t_0 is the start time of data sampling after the flow has established. It is clear in this figure that, at $\varphi = 30°$ and 90°, the velocity fluctuates around a steady mean value while the wake is skewed towards one wall (refer to Fig. 13a and c). In contrast, a sudden drop of the velocity occurs at $t - t_0 \approx 10$ at $\varphi = 60°$, indicating an abrupt change of the wake dynamics. An animation of the flow development around this time shows that initially the wake skews toward Wall B (corresponding to the period of $t - t_0 \approx 0$–10). Then the wake gradually shifts toward the centre of the channel while the amplitude of velocity fluctuation and the mean value of velocity changes

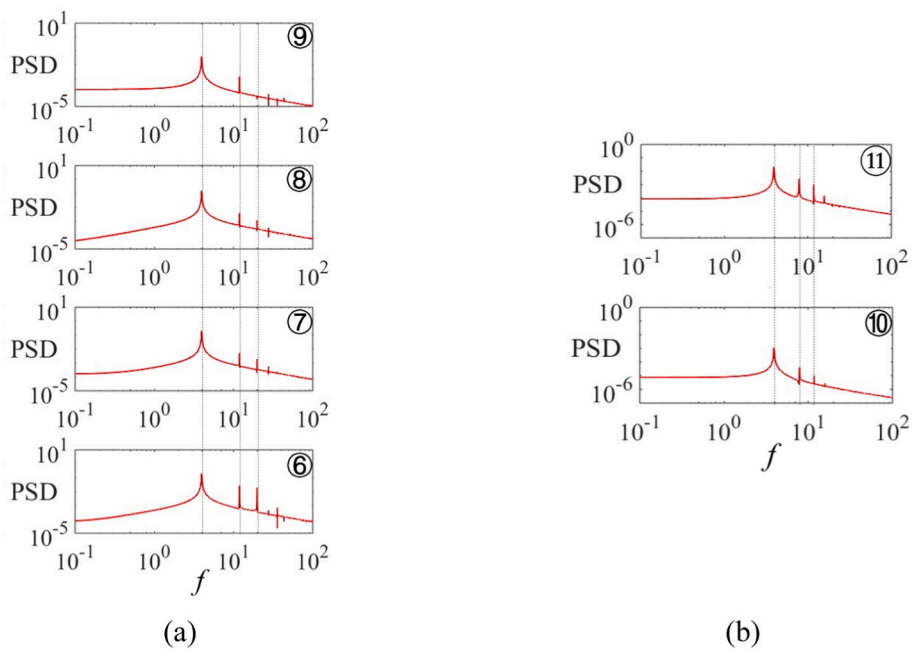

Fig. 11. Power spectra of transverse velocity fluctuations (a) in the wake (⑥~⑨) and (b) in the separated shear layer (⑩~⑪) at $\beta = 0.50$ for $Ra = 6.0 \times 10^{10}$.

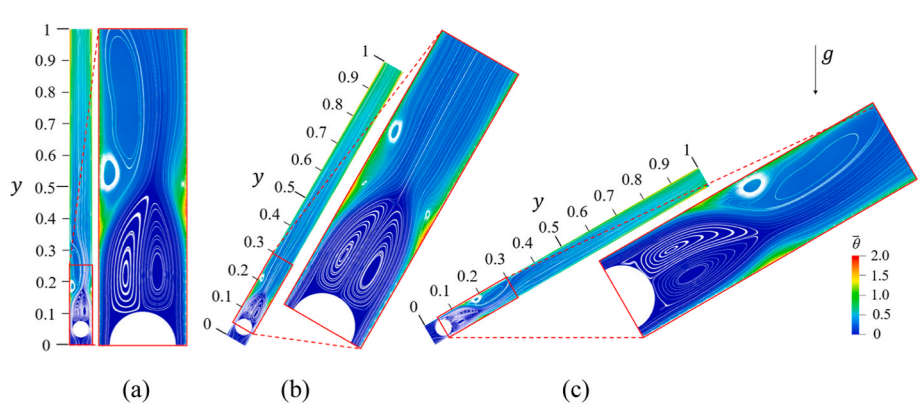

Fig. 12. Time-averaged isotherms and streamlines at $\beta = 0.75$ and $\varphi =$ (a) 90°, (b) 60°, (c) 30° at $Ra = 6.0 \times 10^{11}$.

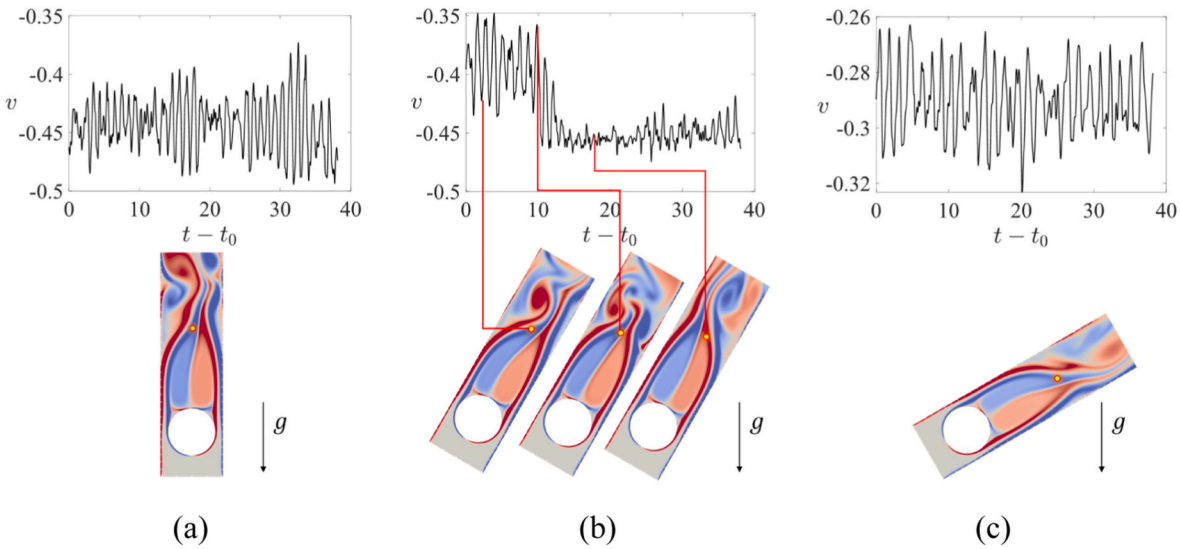

Fig. 13. Time series of longitudinal velocity at a monitoring point $(x, y) = (0, 0.1)$ and instantaneous vorticity contours at $\beta = 0.75$ and $\varphi =$ (a) 90°, (b) 60°, (c) 30° for $Ra = 6.0 \times 10^{11}$.

from high to low. At a certain time, the wake switches the side, skewing toward Wall A. A similar observation has been reported in a direct numerical simulation of non-thermal flows by Lu et al. [22], who observed both spatial (along the spanwise direction) and temporal switches of "wake bias". In another study of TBL adjacent to inclined plates, Sparrow and Husar [23] experimentally observed that the longitudinal rolls (referred to as a secondary flow in their study) in the TBL begin to merge and break down when the inclination angle is reduced to below 55°. Similarly, Ruth et al. [24] and Daniels et al. [25] reported a transition from transverse roll to longitudinal rolls in the TBL adjacent to a bottom heated wall of an inclined channel at certain inclination angle, which may be attributed to secondary flow instabilities. The observed switch of the wake skewness at $\varphi = 60°$ in the present study may also be caused by a secondary flow instability. However, resolving the secondary flow instability is beyond the scope of the present investigation.

Fig. 14 presents contours of time-averaged turbulent buoyancy flux $\overline{\theta' v'}$ and Reynolds stresses $\overline{u'u'}$, $\overline{v'v'}$ and $\overline{u'v'}$ at $\beta = 0.75$ and different inclination angles for $Ra = 6.0 \times 10^{11}$. The results show that, at $\varphi = 30°$ and 90°, a region with high buoyancy flux appears adjacent to Wall A, corresponding to the large recirculation bubble where hot fluid is trapped. High Reynolds normal stress ($\overline{u'u'}$) concentrates near the channel centreline, slightly shifting toward Wall A and extending downstream due to merging of the separated wall shear layers in the wake. In contrast, high Reynolds normal stress ($\overline{v'v'}$) is concentrated near the channel walls, indicating strong longitudinal velocity fluctuations within the TBLs. Both Reynolds normal stresses become weaker in the far wake, which is also the case for the Reynolds shear stress ($\overline{u'v'}$). However, the distribution of the Reynolds shear stress is more spread-out compared to the Reynolds normal stresses.

The dimmish of the asymmetric structure at $\varphi = 60°$ is also evident in Fig. 14 (b). Clearly, the distributions of the turbulent buoyancy flux and Reynolds stresses at $\varphi = 60°$ appear more symmetric compared to those at other inclination angles. High turbulent buoyancy flux regions are present near both channel walls, indicating comparable heat dissipation between the two TBLs. The high-normal-stress ($\overline{u'u'}$) region appears around the channel centreline without shifting to either wall, while an approximately symmetric structure with high Reynolds normal stress ($\overline{v'v'}$) and a "butterfly with two extrema" pattern of the Reynolds shear stress ($\overline{u'v'}$) are observed behind the vortex formation region. The butterfly pattern is similar to that reported by Parnaudeau et al. [26] behind an unconfined circular cylinder in a non-thermal flow at $Re = 3900$ and by Nguyen and Lei [20] behind a confined circular cylinder in a non-thermal flow at $\beta = 0.6$ ($318 < Re < 1431$).

It is worth noting that, in the present model, both channel walls are uniformly heated at an equal strength. Under such configuration, similar flow behaviour and thermal structures are expected if the channel is

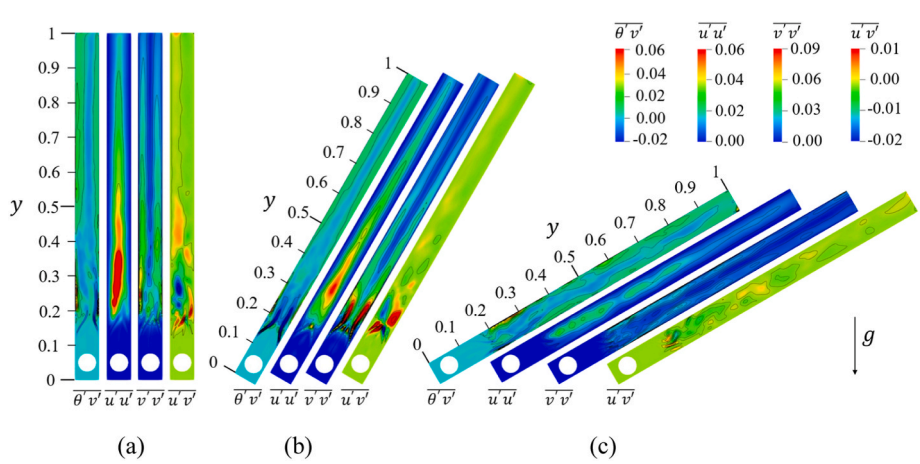

Fig. 14. Time-averaged buoyancy flux and Reynolds stresses $\overline{\theta' v'}$, $\overline{u'u'}$, $\overline{v'v'}$, $\overline{u'v'}$ at $\beta = 0.75$ and $\varphi =$ (a) 90°, (b) 60°, (c) 30° for $Ra = 6.0 \times 10^{11}$.

inclined in the counterclockwise direction.

3.1.4. Effects of cylinder position

The effects of the longitudinal location of the cylinder on flow behaviours are similar at different inclination angles. Accordingly, we consider a fixed inclination angle $\varphi = 30^\circ$ as an example. Fig. 15 illustrates instantaneous vorticity contours with the cylinder placed at different longitudinal positions (h) along the channel. It is seen in this figure that the effects of the cylinder on the channel flow, more specifically, the occurrence of vortex shedding and its effect on downstream thermal boundary layers, are similar for the different cylinder positions. The presence of the cylinder causes separation and reattachment of the wall shear layers. At all cylinder positions, the shear layers separating from the cylinder merge with the wall shear layers, forming a reversed von Kármán vortex street, which is a dominant feature of the wake. As h increases, stronger interactions between the separated shear layers and the TBLs is observed, which is beneficial for dissipating heat and maintaining a relatively low wall temperature (Refer to Section 3.2.3).

3.2. Thermal flow performance

In this section, we examine the time-averaged wall temperatures and the mass flow rate through the flow channel, which are indicators of thermal flow performance. For many applications such as in ventilation channels and building-integrated photovoltaic panels, it is desirable to maximum the mass flow rate through the channel and minimise the wall temperatures. This section aims to unveil the impact of individual control parameters on the overall thermal flow structure and performance in the convective flow channel.

3.2.1. Effects of blockage

Fig. 16 illustrates the time-averaged temperature profiles along both channel walls ($\overline{\theta}_w$) at various blockage ratios and Rayleigh numbers. Fig. 17 (a) plots the ratio of the spatially and temporarily averaged wall temperatures ($\overline{\theta}_{wavg}$) to that of an unblocked channel ($\overline{\theta}_{wavg,0}$) versus the blockage ratio, and Fig. 17 (b) plots the ratio of the mass flow rate ($\dot{m}$) through the channel to that of an unblocked channel ($\dot{m}_0$) versus the blockage ratio. All the data in Figs. 16 and 17 are obtained in a vertical channel with a cylinder located at $h = 0.05$.

It is clear in Fig. 16 that the effect of the cylinder on the wall temperature distribution depends on the Ra. At $Ra = 6.0 \times 10^9$, the blockage disturbs the flow and promotes mixing in the wake, but the wall temperature downstream of the cylinder in the confined channel gradually becomes higher than that in the unblocked channel, particularly at $\beta = 0.75$. This results in an increase of the spatially and temporarily averaged wall temperature (refer to the black curve in Fig. 17 (a). Meanwhile, it can be seen in Fig. 17 (b) that the mass flow rate decreases at all blockage ratios for $Ra = 6.0 \times 10^9$. This occurs because the buoyancy force is relatively weak at this low Ra, and the obstruction effect of the cylinder outpaces its benefit of enhancing mixing. As a result, the overall flow moves slower through the channel, causing a relatively higher wall temperature. The situation is different at higher Ra. As the buoyancy force becomes stronger, the mixing induced by the cylinder becomes predominant. For $Ra = 6.0 \times 10^{10}$ and 6.0×10^{11}, the overall time-averaged wall temperature profiles along the channel walls are lower than that in the unblocked channel at $\beta = 0.25$ and 0.50 (depicted in Fig. 16b and c). At $Ra = 6.0 \times 10^{11}$, a maximum 31 % reduction of the mean wall temperature is achieved at $\beta = 0.50$ (Fig. 17a), while the mass flow rate increases by 40 % at $\beta = 0.25$ (Fig. 17b). This indicates that enhanced thermal flow performance can be achieved by flow blockage at higher Ra.

However, compared to the cases with lower blockage ratios, the "cooling effect" on the wall temperatures is weaker at $\beta = 0.75$. The reduction of the temporally and spatially averaged wall temperature diminishes or becomes less beyond $\beta = 0.50$ due to increased flow obstruction. A surge of the time-averaged wall temperature behind the cylinder ($y \approx 0.2$–0.4) is clearly visible in Fig. 16 (b) and (c) at $\beta = 0.75$ for $Ra = 6.0 \times 10^{10}$ and 6.0×10^{11}. This temperature surge corresponds to the recirculation bubble which traps hot fluid (refer to Section 3.1.1). Further, the temperature profiles of the two lateral walls depart from each other at $\beta = 0.75$, especially at $Ra = 6.0 \times 10^{11}$, which is related to the flow asymmetry at high blockage ratios discussed above.

3.2.2. Effects of inclination

The effects of inclination on the thermal flow performance are consistent across all three Rayleigh numbers, as depicted in Fig. 18. Here, $\overline{\theta}_{wavg,90}$ and $\dot{m}_{90}$ are the temporally and spatially averaged wall temperature and mass flow rate obtained in the corresponding vertical channel ($\varphi = 90^\circ$). It is clear that, as the inclination angle reduces, the mass flow rate decreases while the wall temperature increases, indicating deteriorating thermal performance, especially at relatively low Ra. A 22 % increase of the mean wall temperature and a 25 % drop of the mass flow rate are observed at $\varphi = 30^\circ$ for $Ra = 6.0 \times 10^9$ compared to that in the vertical channel.

3.2.3. Effects of cylinder position

Fig. 19 (a) plots the temperature profiles along the channel wall obtained with the cylinder at various longitudinal positions. It is seen that the wall temperature increases smoothly along the channel upstream of the cylinder, indicating uninterrupted growth of the thermal boundary layer. A significant drop of the wall temperature occurs behind the cylinder because the accelerated flow past through the small gaps results in enhanced local convection. The interactions between the separated shear layers and TBLs further result in increased mixing in the wake of the cylinder. As discussed in Section 3.1.4, the strongest local mixing is observed behind the cylinder when it is located at $h = 0.50$. However, this cylinder position does not lead to an optimal performance in terms of the spatially and temporarily averaged wall temperature

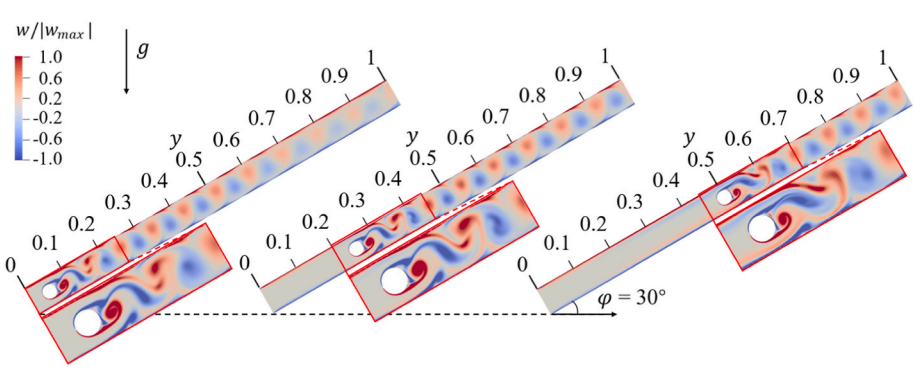

Fig. 15. Instantaneous vorticity contours for different cylinder positions in an inclined channel at $\varphi = 30^\circ$, $\beta = 0.50$ and $Ra = 6.0 \times 10^{11}$. Left to right: $h = 0.05$, 0.25, 0.50.

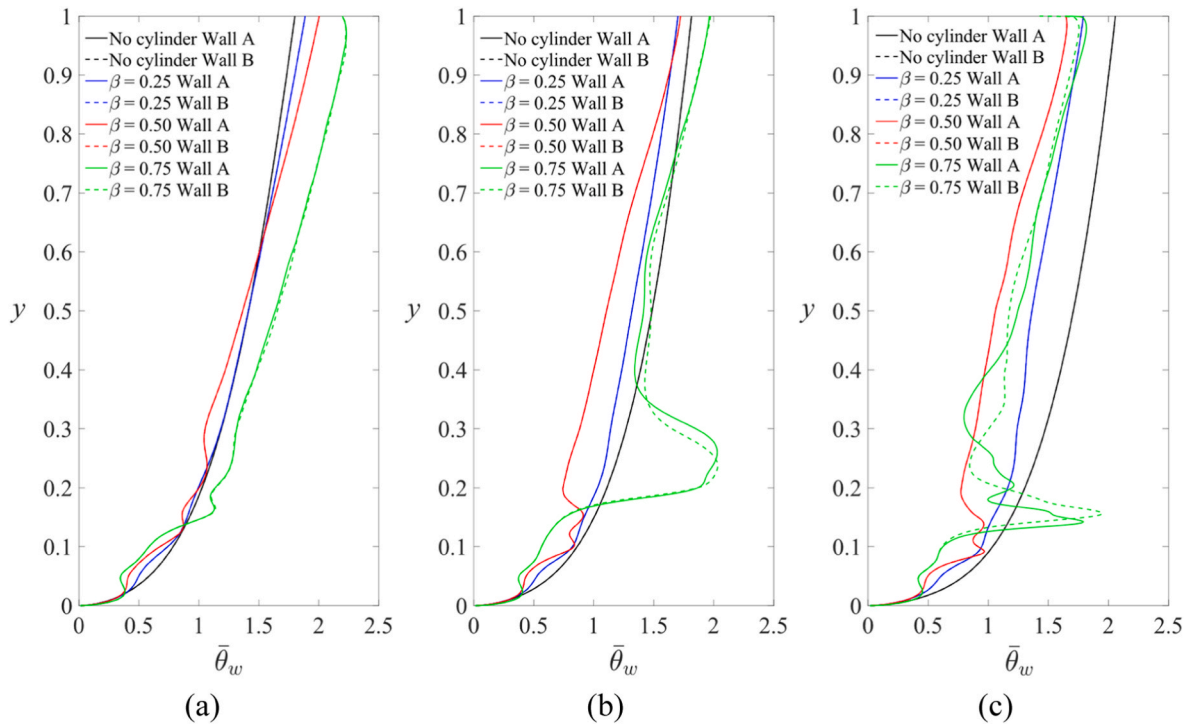

Fig. 16. Time-averaged wall temperature profiles at different blockage ratios for $h = 0.05$ and Ra = (a) 6.0×10^9, (b) 6.0×10^{10}, (c) 6.0×10^{11}.

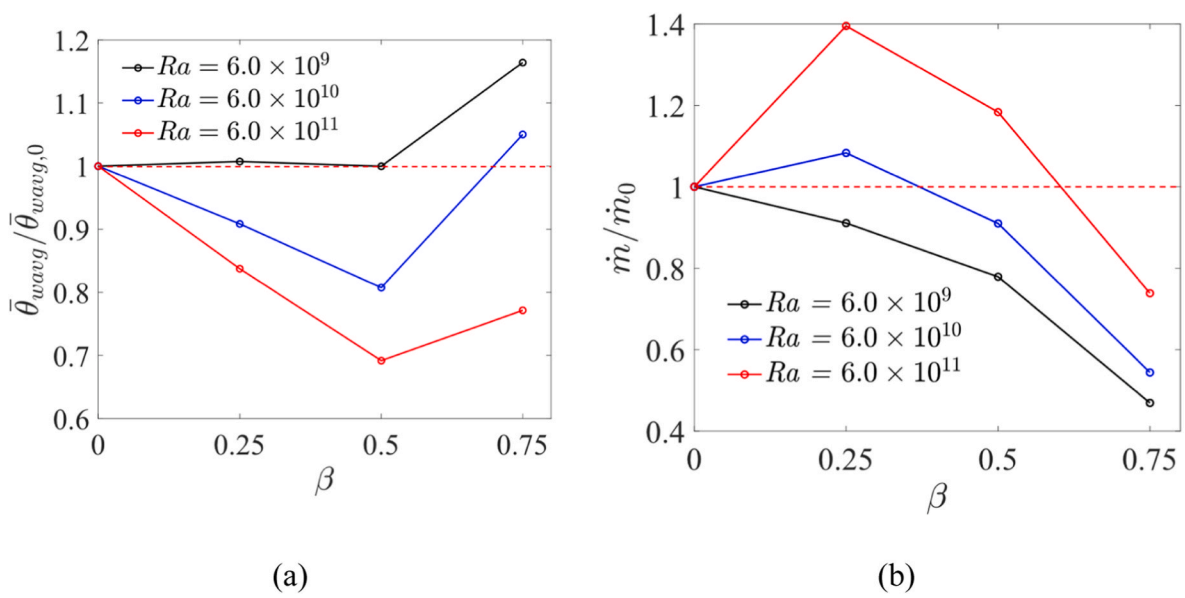

Fig. 17. (a) Spatially and temporarily averaged wall temperatures, and (b) time averaged mass flow rate at different blockage ratios for $h = 0.05$ and different Rayleigh numbers in a vertical channel.

(Fig. 19b). This is because the TBLs are already fully developed upstream of the cylinder, and the downstream region impacted by the presence of the cylinder is limited. The best performance in terms of minimum wall temperature is observed at $h = 0.25$ for all three Ra, and a 29 % reduction of the mean wall temperature is achieved at $Ra = 6.0 \times 10^{11}$. It is worth noting that in an isothermal channel, the overall heat transfer performance is the best when the cylinder is located at $h = 0.05$ [7]. This may be related to different TBL developments under the isothermal and isoflux conditions.

Another noticeable feature of the data presented in Fig. 19 (b) is that, for the lowest Rayleigh number case ($Ra = 6.0 \times 10^9$), the temporarily and spatially averaged wall temperature increases, not decreases, due to the presence of the cylinder regardless of its position. The cause of such distinct behaviour may be due to the relatively weak convection at this Rayleigh number. In this case, the presence of the cylinder tends to obstruct the flow and in turn deteriorate the thermal performance.

Fig. 20 (a) shows the profile of time-averaged longitudinal velocity at the channel outlet. Since the channel is inclined at $\varphi = 30°$, the asymmetry of the longitudinal velocity profile at outlet is distinct. A weak reverse flow (where $\bar{v} < 0$) near Wall B can be observed when the cylinder is placed near the channel entrance ($h = 0.05$). Consistent with the previous observation, the obstruction effect of the cylinder outweighs

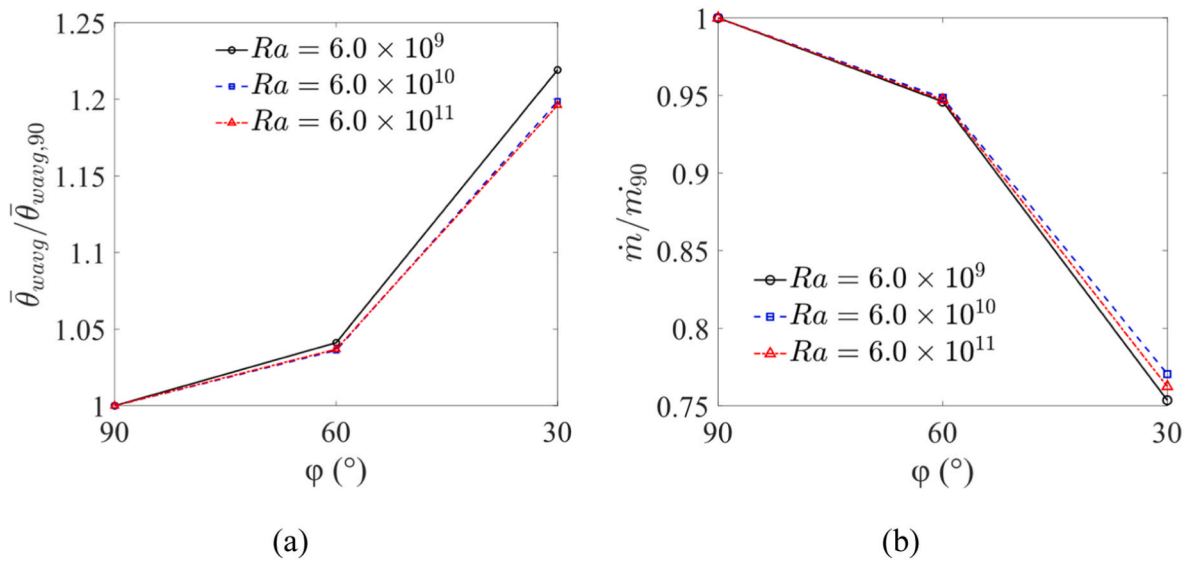

Fig. 18. The time-averaged (a) mean wall temperature. (b) mass flow rate through the channel at $\beta = 0.50$ when $h = 0.05$ for three Rayleigh numbers in inclined channels.

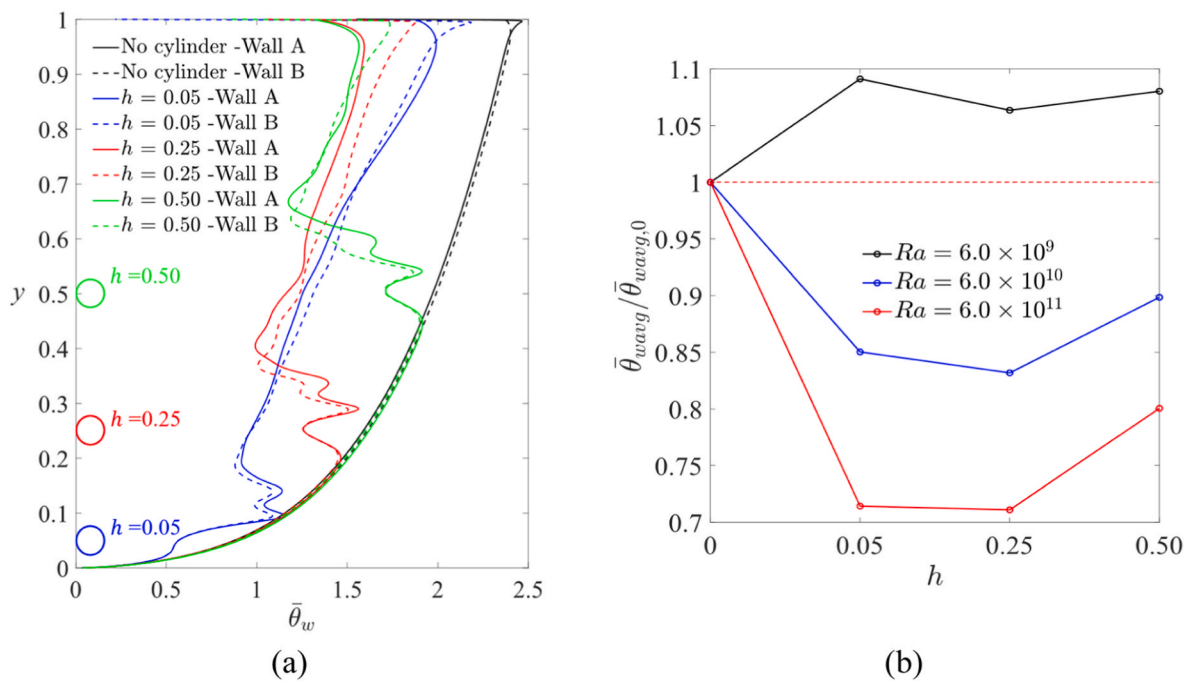

Fig. 19. (a) Time-averaged temperature profiles along both channel walls at $Ra = 6.0 \times 10^{11}$; (b) Spatially and temporarily averaged wall temperature at different Rayleigh numbers. The channel inclination angle is $\varphi = 30°$; and the blockage ratio is $\beta = 0.50$. $h = 0$ represents no cylinder case.

the mixing effect at low Rayleigh numbers. As a result, the mass flow rate through the channel is reduced (refer to Fig. 20b). At $Ra = 6.0 \times 10^{11}$, the mass flow rate increases at $h = 0.05$, but only a 4 % increase of the mass flow rate compared to the unblocked channel is observed. The reduced enhancement is due to weakened convection in the inclined channel compared to the vertical channel. With the cylinder positioned further downstream, the mass flow rate reduces at $h = 0.50$ compared to the unblocked channels.

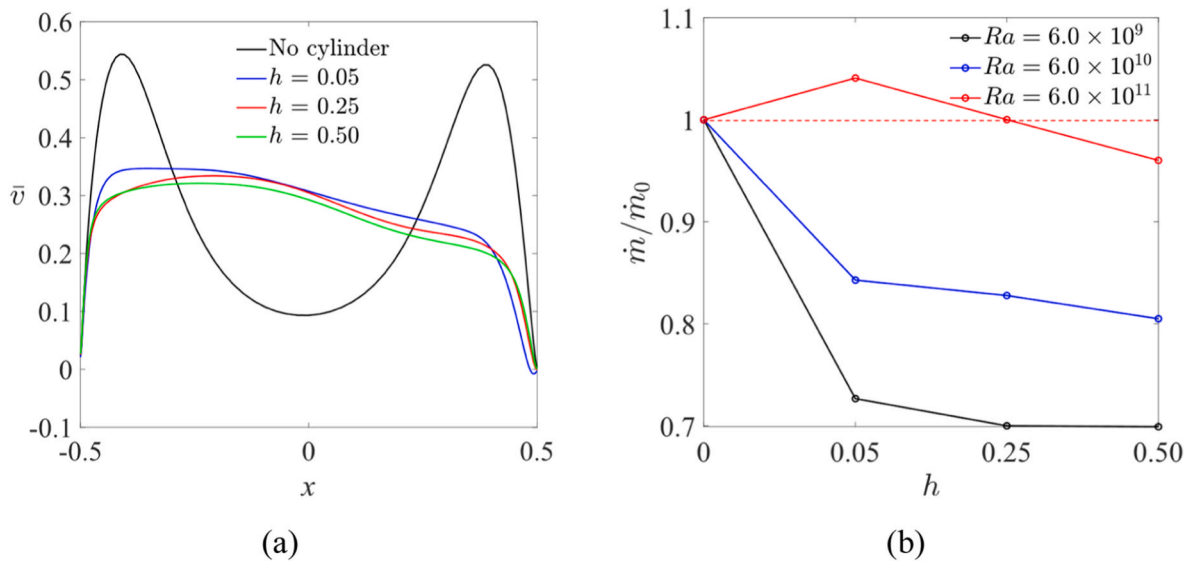

Fig. 20. (a) Time-averaged longitudinal velocity profiles at the outlet of the channel at $Ra = 6.0 \times 10^{11}$; (b) time-averaged mass flow rate. The channel is inclined at $\varphi = 30°$. $h = 0$ represents no cylinder case.

4. Conclusion

The effects of blockage ratio, inclination angle, and the longitudinal position of a circular cylinder on natural convection of air in a uniformly and symmetrically heated channel are comprehensively investigated at different Rayleigh numbers. The present numerical results demonstrate that the blockage ratio has the most critical impact on both the thermal performance and the flow behaviour. At relatively low Rayleigh numbers such as $Ra = 6.0 \times 10^9$, the cylinder obstructs the flow and deteriorates the thermal flow performance due to the relatively weak convection. With increasing Rayleigh numbers, enhanced mixing in the channel due to interactions between vortex shedding behind the cylinder and the TBLs adjacent to the lateral walls outpaces the obstruction effect, leading to a lower average wall temperature and a greater mass flow rate through the channel compared to an unblocked channel. While the thermal performance depends on the cylinder position, the flow structures do not change significantly at different cylinder positions. It is also interesting to note that the symmetry of the time-averaged wake flow structures at the very large blockage ratio of $\beta = 0.75$ is sensitive to the inclination angle.

The results reported here may be used to design a passive strategy with an adiabatic circular cylinder acting as a vortex generator to enhance convective flow in a heated channel and maintain a relatively lower channel wall temperature. Such passive strategy is expected to be more effective for vertical channels and at medium to high Rayleigh numbers.

CRediT authorship contribution statement

Siyu Ji: Writing – review & editing, Writing – original draft, Validation, Methodology, Investigation, Formal analysis, Data curation, Conceptualization. **Quang Duy Nguyen:** Writing – review & editing, Writing – original draft, Validation, Methodology, Investigation, Formal analysis, Data curation, Conceptualization. **Yixiang Gan:** Writing – review & editing, Writing – original draft, Supervision. **Chengwang Lei:** Writing – review & editing, Writing – original draft, Validation, Supervision, Resources, Methodology, Investigation, Funding acquisition, Formal analysis, Data curation, Conceptualization.

Declaration of competing interest

The authors declare that they have no known competing financial interests or personal relationships that could have appeared to influence the work reported in this paper.

Acknowledgements

All numerical simulations were carried out in the high-performance computing facility Artemis at the University of Sydney. This work was supported by the Australian Research Council [Discovery Project grant number DP210102901].

Data availability

Data will be made available on request.

References

[1] S.S. Mousavi Ajarostaghi, M. Zaboli, H. Javadi, B. Badenes, J.F. Urchueguia, A review of recent passive heat transfer enhancement methods, Energies 15 (3) (2022) 986, https://doi.org/10.3390/en15030986.
[2] Q.D. Nguyen, W. Lu, L. Chan, A. Ooi, C. Lei, A state-of-the-art review of flows past confined circular cylinders, Phys. Fluids 35 (7) (2023).
[3] E.M. Sparrow, D.R. Pfeil, Enhancement of natural convection heat transfer from a horizontal cylinder due to vertical shrouding surfaces, J. Heat Tran. 106 (1) (1984) 124–130, https://doi.org/10.1115/1.3246623.
[4] C.F. Marsters, Natural convective heat transfer from a horizontal cylinder in the presence of nearby walls, Can. J. Chem. Eng. 53 (1) (1975) 144–149, https://doi.org/10.1002/cjce.5450530128.
[5] F. Karim, B. Farouk, I. Namer, Natural convection heat transfer from a horizontal cylinder between vertical confining adiabatic walls, J. Heat Tran. 108 (2) (1986) 291–298, https://doi.org/10.1115/1.3246918.
[6] P. Mathis, Heat Transfer Enhancement in Natural Convective Channel Flows by Vortex Streets, RWTH Aachen University, 2022. Thesis, E.ON Energy Research Center.
[7] Q.D. Nguyen, S. Ji, C. Lei, A numerical study of natural convection through a vertical heated channel with a confined circular cylinder, Phys. Fluids 36 (3) (2024) 033628, https://doi.org/10.1063/5.0201307.
[8] L.F.A. Azevedo, E.M. Sparrow, Natural convection in open-ended inclined channels, J. Heat Tran. 107 (4) (1985) 893–901, https://doi.org/10.1115/1.3247518.
[9] O. Manca, S. Nardini, V. Naso, Experimental Analysis of Natural Convection in a Tilted Channel, University of Tasmania, Hobart, Australia, 1992.
[10] D. Talukdar, C.G. Li, R. Kurose, M. Tsubokura, Numerical investigation of transitional characteristics for natural-convection flow in open-ended inclined channel heated from below, J. Heat Tran. 142 (2020), https://doi.org/10.1115/1.4047741, 112601.
[11] W. Zhang, R. Samtaney, Flow across a circular cylinder in an inclined channel stabilized by buoyancy, Int. J. Fluid Eng. 1 (2) (2024) 024301, https://doi.org/10.1063/5.0201281.

[12] R. Khanal, C. Lei, A scaling investigation of the laminar convective flow in a solar chimney for natural ventilation, Int. J. Heat Fluid Flow 45 (2014) 98–108, https://doi.org/10.1016/j.ijheatfluidflow.2013.11.002.
[13] S.V. Patankar, Numerical Heat Transfer and Fluid Flow, CRC Press, Boca Raton, 1980, https://doi.org/10.1201/9781482234213 [Online]. Available:.
[14] Z.D. Chen, P. Bandopadhayay, J. Halldorsson, C. Byrjalsen, P. Heiselberg, Y. Li, An experimental investigation of a solar chimney model with uniform wall heat flux, Build. Environ. 38 (7) (2003) 893–906, https://doi.org/10.1016/S0360-1323(03)00057-X.
[15] M. Thebault, S. Giroux-Julien, V. Timchenko, C. Ménézo, J. Reizes, Detailed flow development and indicators of transition in a natural convection flow in a vertical channel, Int. J. Heat Mass Tran. 143 (2019) 118502, https://doi.org/10.1016/j.ijheatmasstransfer.2019.118502.
[16] G. Desrayaud, E. Chénier, A. Joulin, A. Bastide, B. Brangeon, J.P. Caltagirone, Y. Cherif, R. Eymard, C. Garnier, S. Giroux-Julien, Y. Harnane, P. Joubert, N. Laaroussi, S. Lassue, P. Le Quéré, R. Li, D. Saury, A. Sergent, S. Xin, A. Zoubir, Benchmark solutions for natural convection flows in vertical channels submitted to different open boundary conditions, Int. J. Therm. Sci. 72 (2013) 18–33, https://doi.org/10.1016/j.ijthermalsci.2013.05.003.
[17] H. Suzuki, Y. Inoue, T. Nishimura, K. Fukutani, K. Suzuki, Unsteady flow in a channel obstructed by a square rod (crisscross motion of vortex), Int. J. Heat Fluid Flow 14 (1) (1993) 2–9, https://doi.org/10.1016/0142-727X(93)90034-K.
[18] M. Sahin, R.G. Owens, A numerical investigation of wall effects up to high blockage ratios on two-dimensional flow past a confined circular cylinder, Phys. Fluids 16 (5) (2004) 1305–1320, https://doi.org/10.1063/1.1668285.
[19] M. Hiwada, I. Mabuchi, Flow behavior and heat transfer around a circular cylinder at high blockage ratios, Transactions of the Japan Society of Mechanical Engineers 46 (409) (1982) 1750–1759, https://doi.org/10.1299/kikaib.46.1750.
[20] Q.D. Nguyen, C. Lei, A particle image velocimetry measurement of flow over a highly confined circular cylinder at 60% blockage ratio, Phys. Fluids 33 (10) (2021) 104111, https://doi.org/10.1063/5.0066606.
[21] A.E. Perry, M.S. Chong, T.T. Lim, The vortex-shedding process behind two-dimensional bluff bodies, J. Fluid Mech. 116 (1982) 77–90, https://doi.org/10.1017/S0022112082000378.
[22] W. Lu, D. Aljubaili, T. Zahtila, L. Chan, A. Ooi, Asymmetric wakes in flows past circular cylinders confined in channels, J. Fluid Mech. 958 (2023) A8, https://doi.org/10.1017/jfm.2023.79.
[23] E.M. Sparrow, R.B. Husar, Longitudinal vortices in natural convection flow on inclined plates, J. Fluid Mech. 37 (2) (1969) 251–255, https://doi.org/10.1017/S0022112069000528.
[24] D.W. Ruth, K.G.T. Hollands, G.D. Raithby, On free convection experiments in inclined air layers heated from below, J. Fluid Mech. 96 (3) (1980) 461–479, https://doi.org/10.1017/S0022112080002224.
[25] K.E. Daniels, B.B. Plapp, E. Bodenschatz, Pattern Formation in inclined layer convection, Phys. Rev. Lett. 84 (23) (2000) 5320–5323, https://doi.org/10.1103/PhysRevLett.84.5320.
[26] P. Parnaudeau, J. Carlier, D. Heitz, E. Lamballais, Experimental and numerical studies of the flow over a circular cylinder at Reynolds number 3900, Phys. Fluids 20 (8) (2008) 085101, https://doi.org/10.1063/1.2957018.